Determination of Oxy and Deoxyhemoglobin Concentrations in Skin Tissue using Spatial Frequency Domain Imaging and Artificial Neural Networks

M.R. Gonçalves[1], B.G. da Silva[1], G.H.S. Alves[2] A.F.G. do Monte[2] and D.M. da Cunha[2]

[1]School of Electrical Engineering, Federal University of Uberlandia, Uberlandia, Brazil
[2] Physics Institute, Federal University of Uberlandia, Uberlandia, Brazil

Abstract— **Spatial frequency domain imaging is an emerging technology that enables rapid, wide-field, and non-invasive chromophore mapping. Essentially, in this technique, a large area of the tissue is illuminated with a spatially modulated light field. The light beam reflected by the tissue depends on its optical properties, so that it can provide information about tissue composition through different chromophore concentrations. In this work, we employed a combination of Principal Component Analysis and Artificial Neural Networks to directly determine oxyhemoglobin and deoxyhemoglobin concentrations in skin tissue from diffuse reflectance values obtained from spatial frequency domain imaging. The database consisted of 850500 samples computed from the Beer's law and Monte Carlo simulations, and it was divided into training, validation, and testing subsets in a 0.7:0.15:0.15 ratio. To reduce overfitting during the network training, Bayesian regularization, based on the Levenberg-Marquardt optimization, was employed. Results showed that the developed model predict values of oxy and deoxyhemoglobin concentrations with a correlation coefficient of 0.997 and 0.982, respectively. The average errors from the expected values were 0.98% and 0.99%, for oxy and deoxyhemoglobin, respectively, with most of the samples showing absolute errors lesser than 4%. The developed model was applied to an *in vivo* study to determine hemoglobin concentrations in the hand of a volunteer. Results indicate that the developed model provides good performance in determining the oxyhemoglobin and deoxyhemoglobin concentrations, and it can be easily applied to *in vivo* measurements, with the potential to aid in the diagnosis of vascular changes in skin tissue.**

Keywords— **Spatial frequency domain imaging, chromophores, artificial neural network, optical properties.**

I. Introduction

The ability of light to penetrate biological tissues, interact with them, and carry their physiological information is the fundamental principle of different medical diagnostic techniques [1]. The evaluation of the processes of light absorption and scattering could be used to define chromophore concentrations, yielding valuable information about tissue health. Hemoglobin is an important protein that transports oxygen throughout the human body and its concentration monitoring can not only predict the success of a flap incision or a burn wound outcome, but it could also be used to monitor the efficiency of some cancer treatments [2]–[4]. During the last years, the technology of Spatial Frequency Domain Imaging (SFDI) has been considered to effectively create functional chromophores maps in a rapid, non-invasive, and wide-field way.

The principle of SFDI is based on the projection of a spatially modulated light beam over the tissue, which interacts with it, and then is captured by a CCD camera [1]. After calibration and demodulation procedures, a set of pixel-by-pixel maps are created, so that they represent the correspondent diffuse reflectance (R_d) values of the tissue at the different spatial frequencies employed. Inversion algorithms are then used to correlate this quantity to the tissue optical properties of absorption and scattering. Finally, a set of linear equations, based on Beer's law, are solved to determine chromophore concentrations [5].

In the last years, machine learning methods have been used to effectively determine chromophore concentrations in a fast and accurate way [6]-[8]. In particular, it has been proposed in literature that Artificial Neural Networks (ANN) could be employed to correlate chromophore concentrations directly from diffuse reflectance measurements in SFDI, which could lead to less computational time for signal processing and minimization of errors [9]. An artificial neural network (ANN) is a machine learning method that can efficiently find relationships within a dataset. Its power relies on the capacity to establish non-linear relationships, being largely used for pattern recognition [10]. Overall, an ANN consists of fully connected layers which are divided between an input layer, an output layer, and hidden layers. Each layer has associated neurons with specific weights and biases that are adjusted at each iteration, according to the training function. After successive iterations, the model tends to converge to a more accurate result [11]. Regarding applications in SFDI, Tsui et al. [12] and Wang et al. [13] employed a feedforward network with two hidden layers to obtain chromophore information from diffuse reflectance spectroscopy. Zhao et al.[9] employed a deep residual network to directly mapping chromophore concentration from R_d values. Others ANN architectures were also employed by different authors in the literature [14], [15].

In this work, we propose a combination of a machine learning model based on Artificial Neural Networks and Principal Component Analysis, for pattern recognition that

directly outputs oxyhemoglobin (HbO_2) and deoxyhemoglobin (Hb) concentrations from diffuse reflectance values in a fast and accurate manner. We also apply the developed model to an *in vivo* study, in order to evaluate its feasibility.

II. Methodology

A. Spatial Frequency Domain Imaging

The principle of SFDI is based on measuring the reflected light beam by a wide area of tissue, when this latter is illuminated with a patterned light field. A simplified model of the SFDI equipment is shown in Figure 1a, and the experimental setup is shown in Figure 1b. A white light source (D555WH, Vivitek®) was used to project a spatially modulated light beam on the tissue. The light beam interacts with the tissue and carries its physiological information. A filter wheel (CFW6, Thorlabs Inc®) selected a given light wavelength, and a CCD camera (DCC3240C Digital Camera, Thorlabs Inc®) was used to capture the signal. In this work, two different wavelengths were employed: 488 and 650 nm, and five spatial frequencies for the incident beam were evaluated: 0, 0.05, 0.1, 0.2, and 0.4 mm^{-1}, and for each one, three different phases were used (0°, 120°, and 240°).

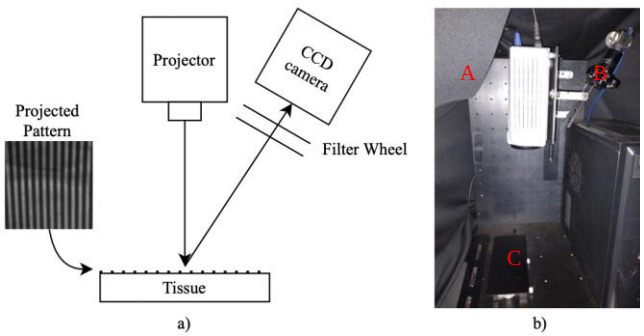

Fig. 1 a) Schematic representation of the SFDI system. b) Experimental setup of the SFDI system from the Functional Imaging Lab (Federal University of Uberlândia): A - Projector; B - CCD camera with a filter wheel attached and C – Target location for positioning the sample.

For each light wavelength value, the image acquisition process consists in obtaining the diffuse reflectance (R_d) of the tissue at the spatial frequencies and phases considered. In this work, the determination of R_d values was based on the methodology proposed by Cuccia et al. [5], which comprises the demodulation and calibration of the images captured by the camera, using an equivalent material simulator (phantom) [6]. At the end of this process, a set of five widefield images are created for each light wavelength, in which each pixel represents a diffuse reflectance value at a given spatial frequency.

B. Skin Model

The optical properties of skin tissue are directly related to its composition and can be defined quantitatively by the absorption and scattering coefficients [11]. These two parameters characterize the interactions of light photons with the tissue, and thus, they determine the behavior of the reflected beam [12]. In this work, the skin tissue was modeled considering oxy and deoxyhemoglobin as the major light absorbers [16]. In particular, the absorption coefficient, μ_a, measures how much the tissue absorbs light and is normally related to tissue metabolic functions [2]. As proposed by Tabassum et al. [2], the coefficient μ_a of the skin at a given light wavelength λ can be computed as:

$$\mu_a(\lambda) = \ln(10)\left(C_{oxi}\varepsilon_{oxi}(\lambda) + C_{deoxi}\varepsilon_{deoxi}(\lambda)\right) \quad [1]$$

where $\varepsilon_{oxi}(\lambda)$ and $\varepsilon_{deoxi}(\lambda)$ are the extinction coefficients of oxyhemoglobin and deoxyhemoglobin, respectively, in units of cm^{-1}/Mol, and C_{oxi} and C_{deoxi} are the respective concentrations of each chromophore, in units of Mol (M). The values of $\varepsilon_{oxi}(\lambda)$ and $\varepsilon_{deoxi}(\lambda)$ employed in this work were obtained from the data compiled by Jacques and Prahl [17].

To simulate real tissue parameters, we varied both hemoglobin and deoxyhemoglobin concentrations within a wide physiological range of 1–300 µM [11]. The reduced scattering coefficient, μ_s', which is related to the probability of a photon to be scattered, was also varied within the limits given in the literature for a human tissue, between 0.5–2.0 mm^{-1} [9], [18]. The samples were organized in a full permutation manner, in order to model different skin compositions as possible [9].

C. Determination of $R_d(\mu_a, \mu_s')$ database

The values of diffuse reflectance R_d for different pairs of coefficients (μ_a, μ_s') were obtained theoretically employing Monte Carlo (MC) simulations for light transport within the tissue. A MC code was developed, following the methodology proposed by Wang et al. [19]. The simulation consisted in projecting a light photon shower on a homogeneous medium characterized by four parameters: the absorption and reduced scattering coefficients μ_a and μ_s', respectively, the index of refraction n and anisotropy factor g. The simulation returned the spatial distribution of the reflected beam, which can be employed for the computation of R_d curves in the spatial frequency domain, through the application of a Fourier transform [6]. Values of R_d at spatial frequencies of 0, 0.05,

0.1, 0.2 and 0.4 mm^{-1} were obtained, for different combinations of μ_a and μ_s' values in the interval $0.001 \leq \mu_a \leq 2.0$ mm^{-1} and $0.5 \leq \mu_s' \leq 2.0$ mm^{-1}. In all cases, a value of $n = 1.4$ and $g = 0.7$ were considered, since they are representative of biological tissues [20]. The database generated with the simulations consisted of a total of 850500 samples, each one representing values of R_d at different spatial frequencies at a given combination of (μ_a, μ_s') values. A surface plot of the values of R_d at a spatial frequency of 0.1 mm^{-1} is shown in figure 2, for different combinations of μ_a and μ_s'.

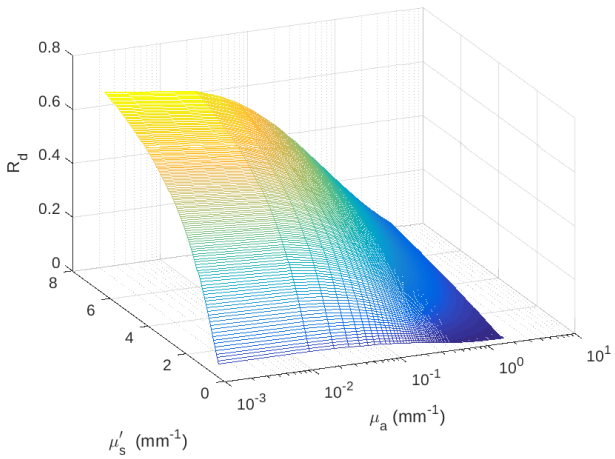

Fig. 2 Surface plot of R_d values at a spatial frequency of 0.1 mm^{-1} for different combinations of optical coefficients μ_a and μ_s'.

D. Data preprocessing

Due to the high dimensionality of the dataset, training an artificial neural network could be challenging and computationally demanding. To address this problem, we employed Principal Component Analysis (PCA), which is a multivariate statistic method for data dimensionality reduction [21]. This multivariate technique identifies new variables (principal components), which are linear combinations of the original variables, that maximize the data variance. In this work, each principal component y_i at a given wavelength was computed as the linear combination of the five values of R_d (one for each spatial frequency), yielding five principal components. The first two components represented 99.9% of the total database variance, and they were kept in our model. The scores of each sample at the first two principal components were then obtained, so that the new database was composed by two components for each wavelength.

Additionally, a min-max normalization was implemented as a feature scaling method, so that sample values at each y_i were rescaled to the interval [0–1], to improve machine learning accuracy [22], [23].

E. Artificial neural network training and testing

Once the database was created and preprocessed, it was used to train the ANN. Different ANN architectures were investigated, by varying the number of hidden layers and neurons in each layer. The ANN architecture adopted in this work consisted of a feedforward artificial neural network with 1 hidden layer and 25 neurons [7]. A model of the ANN is shown schematically in Figure 3. The input layer receives four features: the first and second principal component scores at each wavelength. The output layer returns the concentrations C_{oxy} and C_{deoxy}. Transfer functions of the hidden layer and output layer were hyperbolic tangent activation function and linear transfer function, respectively. The database was separated between training, validation, and testing at a 0.7, 0.15, and 0.15 ratio, respectively. To reduce overfitting, Bayesian regularization backpropagation was employed, which adjusts the weight and bias according to the Levenberg-Marquardt optimization, and the error function considered was the mean squared error [24]. Additionally, for the testing and validation data, a 3% Gaussian noise was applied to the input values. As stopping criteria, 2000 training epochs or a mean squared error value of 10^{-6} were adopted to terminate the training process.

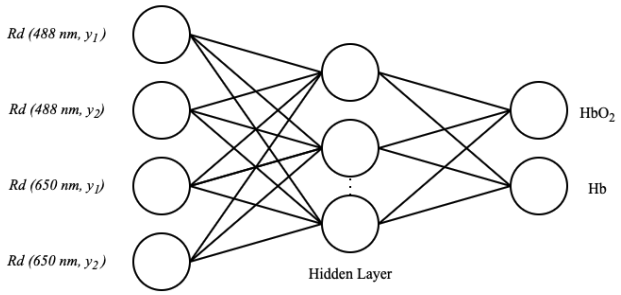

Fig. 3 Simplified model of the ANN. The first and second principal components from the PCA for each wavelength are inputs of the ANN, that directly outputs HbO_2 and Hb concentrations.

F. In vivo study

In order to investigate the feasibility of the proposed model, an *in vivo* study was performed. The dorsal side of a volunteer's male hand was carefully positioned into the SFDI imaging system, and the ANN was used to directly calculate oxyhemoglobin and deoxyhemoglobin concentrations from the measured signal. The *in vivo* study in human beings has been approved by the Research Ethics Committee of the Federal University of Uberlândia (process n. 85363417.9.0000.5152).

III. Results

Figure 4 shows a scatter plot that compares the expected oxyhemoglobin concentration with the values estimated by the ANN. Results refer to the test data.

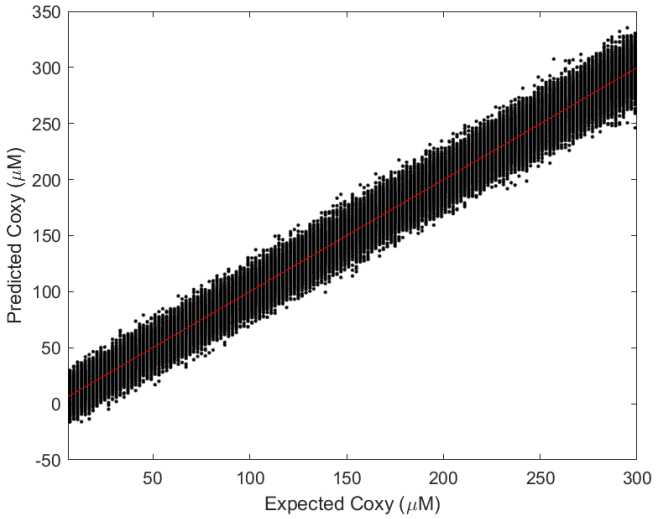

Fig 4. Scatter plot of oxyhemoglobin concentration, comparing the expected values with the estimated values for the test data. The red line represents the expected values, and the black dots are the values estimated by the ANN.

Figure 5 shows the histogram of the relative percentual errors for the test data.

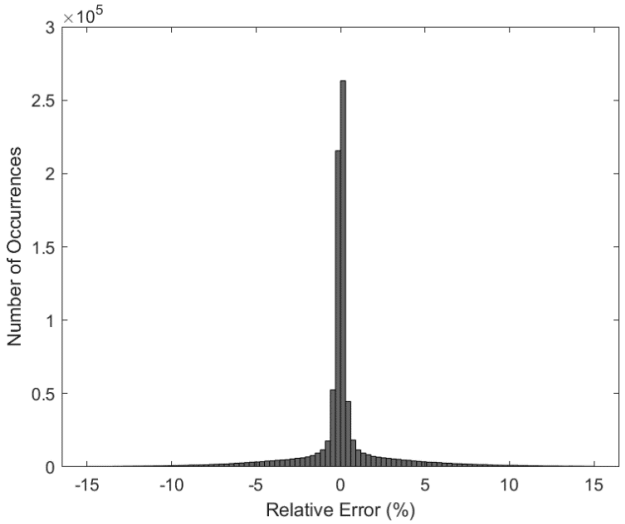

Fig. 5 Relative error distribution of oxyhemoglobin concentration for the test data.

Figure 6 shows a scatter plot that compares the expected deoxyhemoglobin concentration with the values estimated by the ANN. Results refer to the test data.

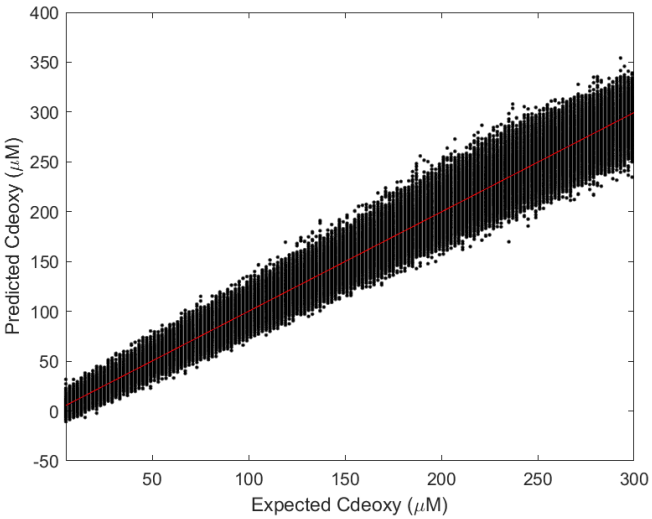

Fig. 6 Scatter plot of deoxyhemoglobin, comparing the expected values with the estimated values. The red line represents the expected values, and the black dots are the values estimated by the ANN.

Figure 7 shows the histogram of error distribution of deoxyhemoglobin concentrations.

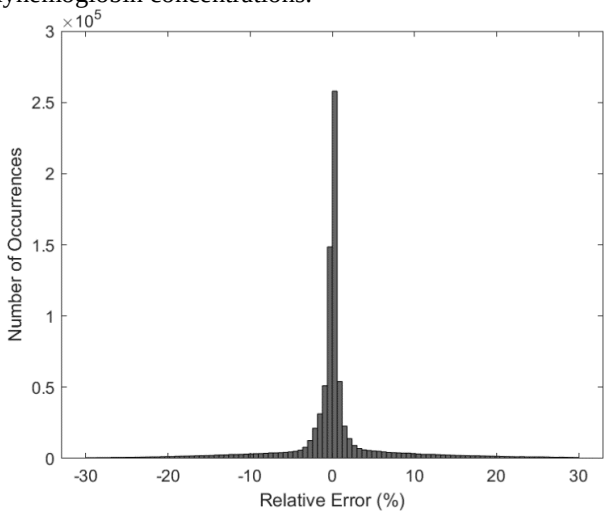

Fig. 7 Relative error distribution of deoxyhemoglobin concentration for the test data.

Figure 8(a) shows the *in vivo* study of the dorsal side of a patient hand, where the red rectangle represents the region of interest (ROI) captured by the CCD camera. Figure 8(b) shows the corresponding oxyhemoglobin concentration map,

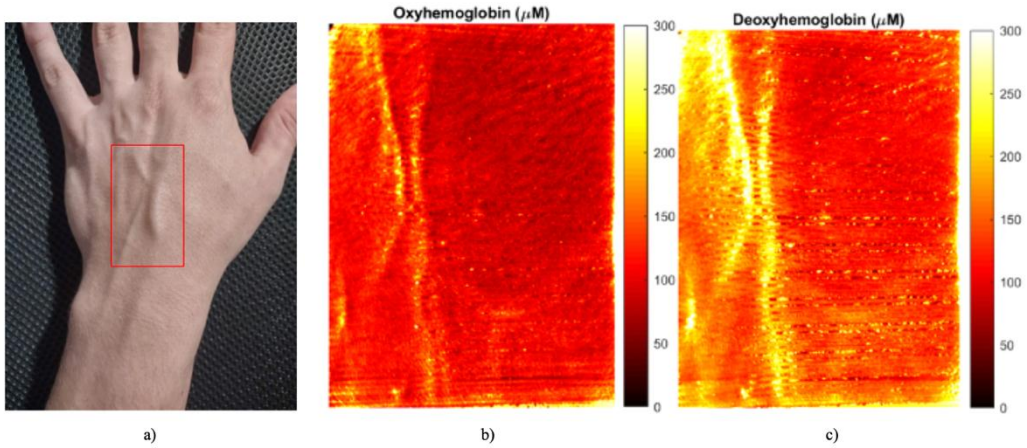

Fig. 8 a) Dorsal side of a patient hand used in the *in vivo* study. The red rectangle represents the imaged ROI. b) Oxyhemoglobin concentration map (μM) of the ROI. c) Deoxyhemoglobin concentration map (μM).

in units of μM, while Figure 8(c) shows the deoxyhemoglobin concentration in μM.

IV. Discussion

Figures 4 and 6 show that the predicted values of oxyhemoglobin and deoxyhemoglobin are highly correlated with the expected values. In fact, the computation of R^2 factor, between predicted and expected values, yielded values of 0.997 and 0.982, for oxy- and deoxyhemoglobin, respectively, indicating a strong correlation between the quantities. From figure 5, it is observed that the average percentual error in predictions of oxyhemoglobin concentration was 0.99%, with 90% of samples lying within the error interval between -2 and 2%. For deoxyhemoglobin, the average error was also 0.98%, with most predicted values lying in the error margin interval between -4 and 4%. These results point to the excellent accuracy and precision of the developed model. They also indicate that simpler ANN architectures could be successfully employed in SFDI in order to obtain chromophore concentrations from diffuse reflectance data, in accordance with recent findings reported by Song et al. [25].

The *in vivo* study shows that the machine learning model can be applied to the SFDI technology, in order to determine hemoglobin concentrations from diffuse reflectance measurements. The concentration maps of oxy and deoxyhemoglobin of the hand of the volunteer, shown in figure 8, represent the vascularization of oxygenated and deoxygenated blood. The oxyhemoglobin concentration in the blood vessels were in the range [200, 250] μM, while values were approximately constant in the rest of the image, which lied in the interval [100, 150] μM. A similar behavior is observed in Figure 8(c), for the deoxyhemoglobin concentration map, which shows values in the range [200, 300] μM for the blood vessels and [150, 200] μM in the remaining tissue. It is known that veins are rich in carbon dioxide and poor in oxygen, due to the conversion of arterial blood to venous blood in the hematosis process [26]. This can be seen in figure 8 as the blood deoxyhemoglobin concentration is higher than the oxyhemoglobin concentration, featuring the venous blood. These results points to the potential of the technique to provide diagnostic information about vascular changes in the skin, which could be related to morphological or physiological tissue alterations, like those observed in different types of skin tumors [27].

V. Conclusions

In this work, we presented a combination of principal component analysis and an artificial neural network model for pattern recognition that accurately determines oxyhemoglobin and deoxyhemoglobin concentrations in skin tissue directly from the diffuse reflectance values, obtained from the SFDI system. To measure the effectiveness of our model, we used the R^2 correlation factor and a histogram of relative errors. For the oxyhemoglobin, a value of 0.997 was obtained for R^2 and the relative errors were mostly concentrated between the interval [-2, 2] % with a 0.99% mean. For the deoxyhemoglobin, the R^2 factor was 0.982 and the errors were concentrated in the [-4, 4] % range with 0.98% average. Additionally, we employed the developed model in an *in vivo* study, showing its feasibility in acquiring functional images of hemoglobin concentration. The obtained results indicate the good accuracy and usability of the model, since images are taken in a wide-field, non-contact, and rapid manner.

These results particularly point to the potential of the technique in supporting physicians in the detection of morphological or physiological changes in vascularization of the skin, which could be related to different tissue abnormalities, for example, as those observed in skin cancer.

Acknowledgment

The authors thank to Brazilian agencies CNPq (Conselho Nacional de Desenvolvimento Científico e Tecnologico) and CAPES (Coordenação de Aperfeiçoamento de Pessoal de Nível Superior), for the concession of the financial support.

Conflict of interest

The authors declare that they have no conflict of interest.

References

1. Gioux S, Mazhar A, Cuccia DJ (2019) Spatial frequency domain imaging in 2019: principles, applications, and perspectives. J Biomed Opt. 24(7): 071613-1 - 071613-18. doi: 10.1117/1.jbo.24.7.071613
2. Tabassum S, Zhao Y, Istfan R et al. (2016) Feasibility of spatial frequency domain imaging (SFDI) for optically characterizing a preclinical oncology model. Biomed Opt Express. 7(10):4154-4170. doi: 10.1364/boe.7.004154
3. Nguyen JT, Lin SJ, Tobias AM et al. (2013) A novel pilot study using spatial frequency domain imaging to assess oxygenation of perforator flaps during reconstructive breast surgery. Ann Plas Surgery. 71:308-315. DOI: 10.1097/SAP.0b013e31828b02fb
4. Kennedy GT, Stone R, Kowalczewski AC et al. (2019) Spatial frequency domain imaging: a quantitative, noninvasive tool for in vivo monitoring of burn wound and skin graft healing. J Biomed Opt. 24(7): 071615-1 – 071615-9. doi: 10.1117/1.jbo.24.7.071615
5. Cuccia DJ, Bevilacqua F, Durkin AJ et al. (2009) Quantitation and mapping of tissue optical properties using modulated imaging. J Biomed Opt. 14(2): 024012-1 - 024012-13. doi: 10.1117/1.3088140
6. Barman I, Dingari NC, Rajaram N et al. (2011) Rapid and accurate determination of tissue optical properties using least-squares support vector machines. Biomed Opt Express. 2(3):592-599. doi: 10.1364/BOE.2.000592
7. Fredriksson I, Larsson M, Strömberg T (2020) Machine learning for direct oxygen saturation and hemoglobin concentration assessment using diffuse reflectance spectroscopy. J Biomed Opt. 25(11): 112905-1 – 112905-16. doi: 10.1117/1.jbo.25.11.112905
8. Smith JT, Ochoa M, Faulkner D, et al. (2022) Deep learning in macroscopic diffuse optical imaging, J Biomed Opt. 27(2): 020901-1 – 020901-26. doi:10.1117/1.jbo.27.2.020901
9. Zhao Y, Deng Y, Yue S, et al. (2021) Direct mapping from diffuse reflectance to chromophore concentrations in multi-fx spatial frequency domain imaging (SFDI) with a deep residual network (DRN). Biomed Opt Express. 12(1): 433 – 443. doi:10.1364/boe.409654
10. Zou J, Han Y, So SS (2008) Overview of artificial neural networks. Method Mol Cell Biol. 458:15-23. doi:10.1007/978-1-60327-101-1_2
11. Jacques SL (2013). Optical properties of biological tissues: A review. Phys Med Biol. 58(14):5007-5008. doi:10.1088/0031-9155/58/14/5007
12. Tsui SY, Wang CY, Huang TH et al. (2018). Modelling spatially-resolved diffuse reflectance spectra of a multi-layered skin model by artificial neural networks trained with Monte Carlo simulations. Biomed Opt Express.; 9(4):1531-1544. doi:10.1364/boe.9.001531
13. Wang CY, Kao TC, Chen YF et al. (2019) Validation of an inverse fitting method of diffuse reflectance spectroscopy to quantify multi-layered skin optical properties. Photonics Res. 6(2): 1-17. doi: 10.3390/photonics/6020061
14. Aguénounon E, Smith JT, Al-Taher M et al. (2020) Real-time, wide-field and high-quality single snapshot imaging of optical properties with profile correction using deep learning. Biomed Opt Express. 11: 5701-5716. doi: 10.1364/boe.39768
15. Chen MT, Durr NJ (2020) Rapid tissue oxygenation mapping from snapshot structured-light images with adversarial deep learning. J Biomed Opt. 25(11): 112907-1 – 112907-12. doi: 10.1117/1.jbo.25.11.112907
16. Wirkert SJ, Kenngott H, Mayer B, et al. (2016) Robust near real-time estimation of physiological parameters from megapixel multispectral images with inverse Monte Carlo and random forest regression. Int J Comput Ass Rad. 11(6):909-917. doi:10.1007/s11548-016-1376-5
17. Jacques S and Prahl S (2018) at https://omlc.org/index.html
18. Lister T, Wright PA, Chappell PH (2012) Optical properties of human skin. J Biomed Opt. 17(9): 090901-1 – 090901-15. doi:10.1117/1.jbo.17.9.0909
19. Wang L, Jacquesa SL, Zhengb L (1995) CML-Monte Carlo Modeling of Light Transport in Multi-layered Tissues. Comput Meth Prog Bio. 47:131-146. doi: 10.1016/0169-2607(95)01640-F
20. Yudovsky D, Durkin AJ (2011) Spatial frequency domain spectroscopy of two layer media. J Biomed Opt.16(10):107005. doi:10.1117/1.3640814
21. Abdi H, Williams LJ (2010) Principal component analysis. Wires Comput Stat. 2(4):433-459. doi:10.1002/wics.101
22. Bishop CM (1995) Neural Networks for Pattern Recognition. Clarendon Press, Oxford
23. Shanker M, HU MY, Hung MS (1996). Effect of Data Standarization on Neural Network Training. Int J Mgmt Sci. 24(4):385-397. doi:10.1016/0305-0483(96)00010-2
24. Burden F, Winkler D (2008) Bayesian Regularization for Neural Networks. Method Mol Bio. 458:25-44. doi: 10.1007/978-1-60327-101-1_3
25. Song B, Jia W, Zhao Y et al. (2022) Ultracompact Deep Neural Network for Ultrafast Optical Property Extraction in Spatial Frequency Domain Imaging (SFDI). Photonics Res. 9(5): 1-12. doi: 10.3390/photonics9050327
26. Rieser TM (2013) Arterial and Venous Blood Gas Analyses. Top Companion Anim M. 28(3):86-90. doi: 10.1053/j.tcam.2013.04.002
27. Kreusch J (2002) Vascular Patterns in Skin Tumors. Clin Dermatol. 20:248-254. doi: 10.1053/j.tcam.2013.04.002

Enter the information of the corresponding author:

Author: Diego Merigue da Cunha
Institute: Instituto de Física
Street: Av. João Naves de Ávila – 2121, Campus Santa Mônica
City: Uberlândia
Country: Brazil
Email: dmerigue@ufu.br